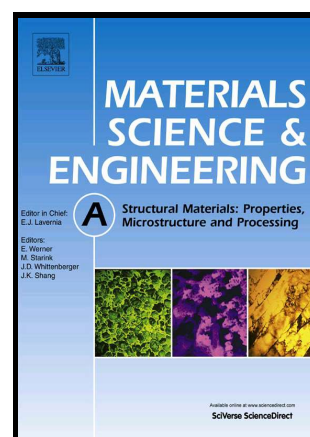Author's Accepted Manuscript

Fracture toughness of hydrogen charged as-quenched ultra-high-strength steels at low temperatures

Sakari Pallaspuro, Haiyang Yu, Anna Kisko, David Porter, Zhiliang Zhang

MATERIALS SCIENCE & ENGINEERING
A
Structural Materials: Properties, Microstructure and Processing

Editor in Chief:
E.J. Lavernia

Editors:
E. Werner
M. Starink
J.D. Whittenberger
J.K. Shang

Available online at www.sciencedirect.com
SciVerse ScienceDirect

www.elsevier.com/locate/msea

Cite this article as: Sakari Pallaspuro, Haiyang Yu, Anna Kisko, David Porter and Zhiliang Zhang, Fracture toughness of hydrogen charged as-quenched ultra-high-strength steels at low temperatures, *Materials Science & Engineering A* http://dx.doi.org/10.1016/j.msea.2017.02.007

This is a PDF file of an unedited manuscript that has been accepted for publication. As a service to our customers we are providing this early version of the manuscript. The manuscript will undergo copyediting, typesetting, and review of the resulting galley proof before it is published in its final citable form. Please note that during the production process errors may be discovered which could affect the content, and all legal disclaimers that apply to the journal pertain.

Fracture toughness of hydrogen charged as-quenched ultra-high-strength steels at low temperatures

Sakari Pallaspuro[a,*], Haiyang Yu[b], Anna Kisko[a], David Porter[a] and Zhiliang Zhang[b]

[a] Materials and Production Engineering, Centre for Advanced Steels Research, University of Oulu, Finland

[b] Department of Structural Engineering, Faculty of Engineering Science and Technology, NTNU, Norway

* corresponding author; sakari.pallaspuro@oulu.fi, Sakari Pallaspuro, Materials and Production Engineering, University of Oulu, PL 8000, 90014 Oulun yliopisto, Finland

ABSTRACT

The effect of hydrogen on the fracture and impact toughness of ultra-high-strength steels at sub-zero temperatures in the transition temperature region has been investigated with arctic applications in mind. Two types of as-quenched microstructure were studied, i.e. autotempered martensite and a mixture of martensite and bainite, both having yield strengths close to 1000 MPa. These were charged with hydrogen using passive cathodic protection and then tested in both the charged and uncharged condition at sub-zero temperatures. Hydrogen contents were measured with melt-extraction. Fractography, kernel average misorientation measurements and cohesive zone modelling were used to analyse the results considering the degree and the active mechanisms of hydrogen embrittlement. It is shown that hydrogen embrittlement is present at sub-zero temperatures, causing an increase in fracture toughness reference temperature T_0 and a small decrease in deformation capability. The relationship between the T_0 and the impact toughness transition temperature T_{28J}, which, in the case of ultra-high-strength steel, deviates from that observed for lower strength steels, is proposed to be affected by the hydrogen content.

Keywords: Hydrogen embrittlement; Fracture toughness; Martensite; Sub-zero; Cohesive zone modelling; Kernel average misorientation

Nomenclature

δ_c	critical cohesive separation
σ_{11}	opening stress
σ_c	critical cohesive stress
$\sigma_{c,H=0}$	hydrogen free critical cohesive stress
σ_v	viscosity regularized cohesive stress
σ_{YS}	yield strength
σ_{TS}	tensile strength
ζ	viscosity parameter
A	elongation
A_g	uniform elongation
C_I	initial, homogeneous hydrogen concentration
C_L	lattice hydrogen concentration
CZM	cohesive zone modelling

CVN	charpy v-notch
d	displacement rate
D_{eff}	effective diffusion coefficient
EBSD	electron backscatter diffraction
F_{max}	maximum force
H	hydrogen
$H_{c,D0.8}$	critical H content that lowers ductility to 80 %
HDL	hydrogen degradation law
HE	hydrogen embrittlement
HEDE	hydrogen enhanced decohesion
HELP	hydrogen enhanced localized plasticity
HV_{10}	Vickers hardness
L-T	Longitudinal – Transverse
KAM	kernel average misorientation
PAG	prior austenite grain
R	gas constant
SENB	single-edge notched bending specimen
T_0	fracture toughness reference temperature
T_{28J}	impact toughness transition temperature
T^z	absolute zero temperature
TSL	traction-separation law
UHSS	ultra-high-strength steel
V_H	partial molar volume of hydrogen

_____

1. INTRODUCTION

Direct-quenched martensitic steels used in the as-quenched condition are a new type of ultra-high-strength structural material with yield strengths above 900 MPa that have emerged in an industrial scale in this century [1]. These steels possess adequate toughness, weldability and formability without tempering and they are typically used in weight-critical mobile structural members [2,3]. Thinner wall thicknesses in yield strength levels of 960 MPa and above can allow weight-savings up to 40 to 60 % under tensile and bending loads compared to conventional S355 steel. By using less material or producing stronger structures it is possible to design more efficient and environmentally sound structures. However, lack of design rules for structural steels with yield strength over 700 MPa [4] limits the full exploitation of these steels at the moment.

A common feature of low-carbon as-quenched steels is that they do not obey the conventional form of the correlation originally introduced in [5] between the fracture toughness reference temperature T_0 and impact toughness transition temperature T_{28J}, i.e. $T_0 = T_{28J} - 18\ °C$ [6–8]. This correlation is used in Eurocode 3 [9] and in the established structural integrity procedures of SINTAP [10] and FITNET [11], so research is needed to evaluate the low-temperature toughness properties of direct-quenched steels, especially with a view to their use in arctic applications.

Wallin et al. [8] have proposed updates to the current version of the Master Curve [12] as well as to the $T_0 - T_{28J}$ correlation that take into account both low-strength and as-quenched ultra-high-strength steels (UHSS) satisfactorily.

But with higher yield strength comes also increased susceptibility to hydrogen embrittlement (HE) [13–18], which characteristically leads to the degradation of the mechanical properties of normally ductile material in the presence of a sufficient hydrogen content, usually by a time-dependent and thermally activated process. The level of degradation is dependent on the local hydrogen concentration and hydrostatic stress in addition to material-specific microstructural factors. In lath-martensitic steel structures all three aspects are combined with high stress levels that translate to larger lattice expansion and faster hydrogen diffusion into the stressed areas and a microstructure with very high density of both weak and strong hydrogen traps, e.g. carbides and dislocations together with grain and sub-grain boundaries (packets, blocks and laths) as described by Morito et al. [19], that translate to high effective solubility of hydrogen.

These microstructural factors affect the rate of diffusion of hydrogen to the areas under tensile stresses. The effective hydrogen diffusion rate is characterized by the effective diffusion coefficient D_{eff}, which can be described by a temperature dependent Arrhenius equation. A problem with studies considering HE in ductile-brittle transition temperature region is, known to authors, that reported diffusion coefficients lower-bound to room-temperature. The lowest temperature where HE tests on steels have been done is the subsea-relevant temperature +4 °C [18]. HE experiments have also been limited to relatively slow strain rates. All three limitations are understandable since HE manifests itself usually by failure in a delayed manner due to the time needed for hydrogen to accumulate to critical levels.

Attempts to quantify the relationship between hydrogen embrittlement in UHSS and mechanical properties have been made. The degradation of the notch tensile strength of tempered martensite as a function of diffusible hydrogen content was found to obey a power law type of behaviour [17]. Similar findings about toughness have been reported by Tvrdy et al. [13] who reported that the static threshold fracture toughness value of UHSS dropped from around 80 to a level of 20 MPa√m in 0.5 M NaCl solution. Based on the loss of ductility linear relationship has been established for as-quenched and quenched and low-temperature tempered steels between tensile strength and the critical total hydrogen content that is needed to lower the elongation to fracture by 20 % ($H_{cD0.8}$) [15,16]. This relationship corresponding to Eq. (1) as well as the trend between strength and critical hydrogen content for a premature fracture for quenched and tempered and as-quenched martensitic steels is shown in Fig. 1.
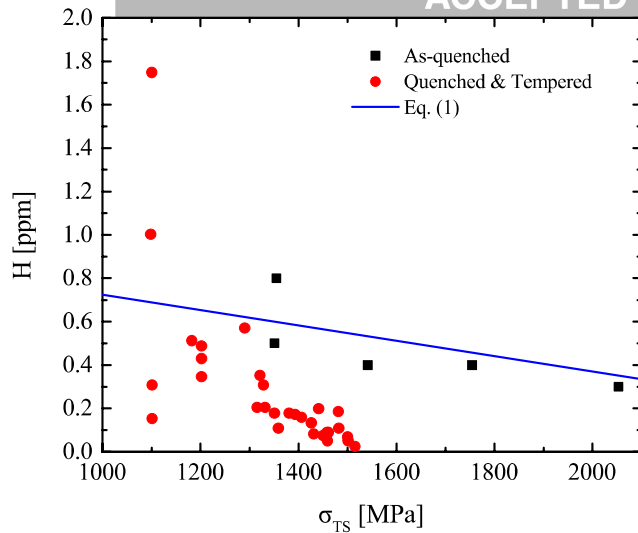
Fig. 1. Critical total hydrogen content for a premature fracture as a function of tensile strength in as-quenched and quenched and tempered microstructures. [14–16]

$$H_{cD0.8} = 1.08 - 3.54 \times 10^{-4} \sigma_{TS} \tag{1}$$

While the detrimental effect of hydrogen on mechanical properties is clear, the mechanisms behind it are more controversial partially due to the multitude of microstructural and environmental factors and loading properties. The two most well established models for hydrogen embrittlement are hydrogen enhanced decohesion (HEDE) and hydrogen enhanced localized plasticity (HELP) that both regard the requirement for failure as a critical combination of hydrogen concentration, stress and strain but differ in the mechanisms. HEDE is based on the hypothesis that hydrogen reduces the cohesive force in atomic bonds and thus lowers the energy needed to separate grain boundaries or cleavage planes [20] and it is generally linked to the presence of brittle intergranular fracture. The mechanism of HELP, on the other hand, is based on observations that solute hydrogen eases dislocation motion and hence increases plastic deformation ahead of the advancing crack tip such that the fracture surface shows localized plastic behaviour while remaining macroscopically brittle [21].

These two mechanisms, HEDE and HELP, and hydrogen embrittlement in general are typically associated with intergranular fracture, quasi-cleavage and "flat" features that are all observed in lath-martensitic steels [17,22–26]. Intergranular fracture, which is usually present in tempered microstructures, propagates along prior austenite grain boundaries and is considered as brittle [27]. Quasi-cleavage, on the other hand, while often misinterpreted as cleavage fracture or used to describe a combination of brittle and ductile features, involves a cleavage-like crack initiating and propagating along {110} slip planes, as opposed to {100} cleavage planes, by the growth and coalescence of shallow voids forming between or in slip bands with very fine, highly deformed tear ridges between them [28]. A quasi-cleavage fracture surface can show lath-sized features [22] as opposed to the effective grain size features of lath-martensitic steels usually seen with cleaveage, where effective grain size is defined as the distance between high-angle grain boundaries. Martin et al. [29] found that hydrogen-related local "flat" features followed prior austenite grain boundaries and consisted of undulating surfaces covered with nano-scale mounds with a highly dislocated microstructure beneath the surface [22,23]. Similar fracture surfaces have also been reported to be transgranular

following {110} slip planes [26]. Nagao et al. [22] observed intense slip deformation under both hydrogen charged "flat" features and quasi-cleavage fracture but no deformation under true cleavage fracture surface and concluded that hydrogen-related crack growth was due to a hydrogen-enhanced and plasticity-mediated decohesion mechanism. The conclusion about the relationships between fracture types and the mechanisms behind them is still far from being resolved; however, it can be seen that in complex steel microstructures the hydrogen-related crack path is controlled by the local case-dependent weakest links.

To measure the hydrogen-influenced plasticity or lattice distortion, an electron backscatter diffraction (EBSD) based kernel average misorientation (KAM) method can be used [30–33]. KAM provides information about the change in local variations in lattice orientation. In this method, the misorientation between a data point at the centre of the kernel and the points at its hexagonal perimeter are measured. The local misorientation value of the centre point is the average of these misorientations. Grain boundaries are excluded from the calculation by setting an upper tolerance bound for the included misorientation. Local misorientation is also sensitive to the choice between all points versus perimeter points in the kernel, to the size of the scan step size and the kernel size, all of which affect the resolution of the analysis. KAM gives a qualitative measure of strain that can be used to compare the amounts of deformation observed under fracture surfaces, as shown in Refs. [32,33].

A method to simulate hydrogen embrittlement is a hydrogen-informed three-step procedure including cohesive zone modelling (CZM) developed in Ref. [34,35]. CZM is a phenomenological representation of the fracture process with interfacial separation. In this approach, the fracture process zone ahead of the crack tip is modelled by inserting cohesive elements on the anticipated crack path between solid elements. The behaviour of these cohesive elements is described with a traction-separation law (TSL) which is characterized by the cohesive strength, or the critical cohesive stress σ_c, and the critical cohesive separation δ_c. The area below the TSL curve corresponds to the cohesive energy. The cohesive parameters can be calibrated according to the experimental results. For more details regarding CZM, the reader is referred to Ref. [36]. The effects of HE can be incorporated into the CZM procedure by lowering the value of σ_c with increasing hydrogen concentration while keeping δ_c constant [37]. The degradation of σ_c is described with a hydrogen degradation law (HDL), which plays a fundamental part in capturing the HE phenomena. Recently, Yu et al. [38] calibrated a CZM-based uniform HDL for an engineering size scale from notched tensile tests using quenched and tempered AISI 4135 steel (Eq. 2), where $\sigma_{c,H=0}$ is the hydrogen free critical cohesive stress and C_L the lattice hydrogen concentration.

$$\frac{\sigma_c}{\sigma_{c,H=0}} = 0.421e^{-2.227 \cdot C_L} + 0.579 \tag{2}$$

In the present study, the susceptibility to hydrogen embrittlement in two ultra-high-strength steels is investigated in sub-zero temperatures using standard fracture toughness and impact toughness tests. The relationship between the transition temperatures, T_0 and T_{28J}, is studied with different hydrogen contents. One aim of the research is to explore whether the deviation of direct quenched steels from the normally observed correlation might be explained by the differing effects of hydrogen on the two transition temperatures; the absence of tempering can be expected to leave higher hydrogen contents in direct quenched steels, which might lead to an increase in T_0 but no increase in T_{28J}. To measure and model the hydrogen-related plasticity and crack growth, two state of the art techniques are used to

complement toughness test results: the kernel average misorientation method for experimental measurement and cohesive zone modelling for numerical simulation.

2. Materials & Methods

2.1. Materials

Two steel microstructures were produced by laboratory heat treating S960QL standard grade steel plates with a chemical composition (in wt. %) of 0.15C-0.3Si-1.2Mn-0.5Cr-0.4Ni-0.5Mo. All the plates were first hydrogen annealed at 600 °C for 4 hours and then austenitized at 900 °C for 45 minutes. After the austenitization, material ATM was produced by quenching in water resulting in an as-quenched autotempered lath-martensitic microstructure. Material AB comprising a mixture of approximately 70% martensite and 30 % bainite (mainly upper bainitic features and some lower bainite) was produced by interrupted quenching to 500 °C, holding 10 seconds in air and then water-quenching to room temperature, Fig. 2. The mixed microstructure of AB, that is also of industrial importance [2,3], was had with the aim of investigating whether the larger carbide surface area of the bainite would result in higher H content and differing proneness to HE due to higher trapping capability. Prior austenite grain (PAG) size is 9 µm (s.d. ‹ 5 %) in both microstructures. Measured tensile properties and average through-thickness hardness values of these materials are presented in Table 1.
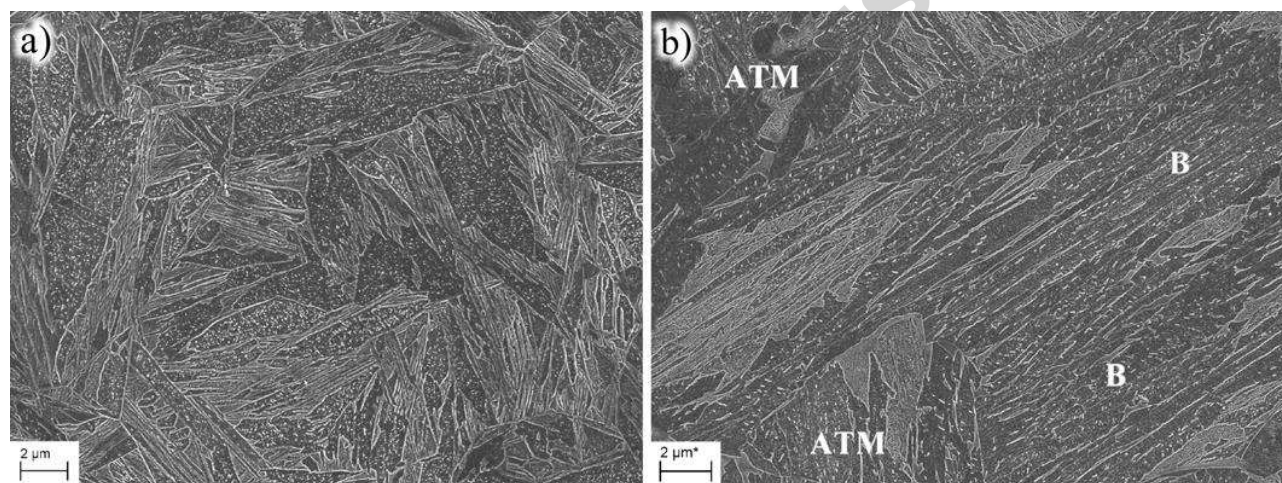

Fig. 2. a) Auto-tempered lath-martensite of the material ATM and b) bainite dominant region of the material AB showing martensite (ATM) and bainite (B).

Table 1. Mechanical properties of the test materials (yield strength σ_{YS}, tensile strength σ_{TS}, total elongation A, uniform elongation A_g and Vickers hardness HV_{10}).

	σ_{YS} [MPa]	σ_{TS} [MPa]	A [%]	A_g [%]	HV_{10}
ATM	1027	1354	13.8	3.7	425
AB	975	1315	13.5	3.8	423

2.2. Hydrogen charging and melt-extraction

To produce a distinctively higher hydrogen content than the initial dehydrogenized condition, room temperature passive cathodic protection was utilised. In cathodic protection corrosion is prevented by converting all the active

(anodic) sites of the steel surface to passive (cathodic) sites by supplying free electrons from an alternative source. In this case aluminium was used as a galvanic sacrificial anode. Atomic hydrogen, a by-product of cathodic protection, readily absorbs into the protected metal causing hydrogen build-up in the steel specimens. A charging arrangement was built by connecting a block of aluminium to the specimens with spot-welded welding wires. This setup was immersed in an electrolyte comprising distilled water + 0.5 M (3.5 wt.%) NaCl. The potential of the system measured against a standard reference electrode (Ag/Ag+) showed a potential of approximately -1050 mV. A charging time of 94 hours was applied in all cases and the specimens were rinsed after the charging and immersed in liquid nitrogen to prevent the diffusion of hydrogen out of the samples.

Small pieces (8 x 8 x 2.5 mm) weighing 1 g were used for both the hydrogen charging trials and melt-extraction to measure the actual hydrogen content in uncharged and charged conditions. These pieces were bolted together with an M3 bolt which was connected to the Al anode. These trial pieces sized to the capacity of a melt-extractor were used to exclude hydrogen leak-out after the charging, which would be a problem if small specimens were cut from larger fracture toughness or Charpy V specimens. After the disconnection from the charging setup the pieces were kept in sub-zero temperatures using liquid nitrogen, also during the polishing before the melt-extraction. Total hydrogen contents were determined for uncharged and hydrogen charged conditions using a Juwe H-mat 225 and melt-extraction at 1550 °C. Based on three measurements per case, H contents were on average 0.6 and 1.1 weight ppm for ATM and 0.9 and 1.4 weight ppm for AB in the uncharged and hydrogen charged conditions, respectively (Fig. 3). The unexpectedly high hydrogen contents in uncharged pieces are most likely due to insufficient hydrogen annealing or accumulation during the five months between the heat treatments and the charging testing experiments. However, the two H levels are significantly different in both materials as tested with one-tailed t-test (p-values $\leq$ 0.029) and thus comparable, even though the target of very low H content in the uncharged materials was not achieved.
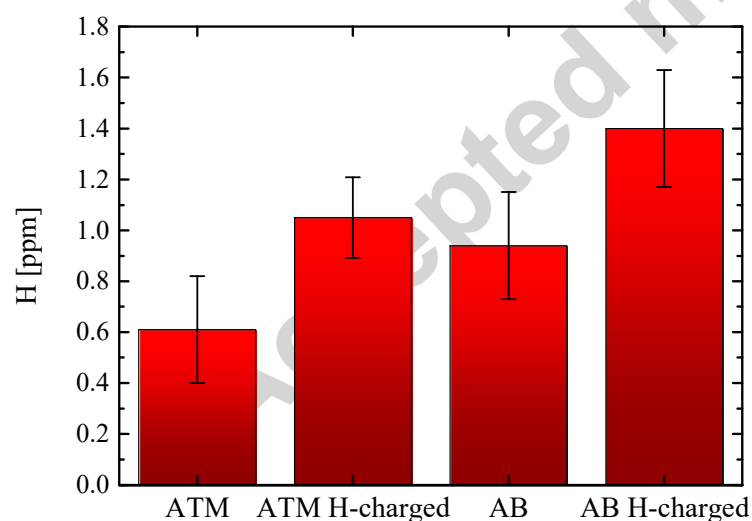

Fig. 3. Measured total hydrogen contents in the uncharged and hydrogen charged conditions with 90 % confidence limits.

2.3. Toughness tests

Fracture toughness and impact toughness tests were used to describe the ductile-brittle transition temperature behaviour of the materials under given H concentrations and to determine the fracture toughness reference temperature T_0 [12]

and the impact toughness transition temperature T_{28J}. (T_0 is the temperature at which $K_{Jc} = 100$ MPA√m, later referred also as transition temperature). L-T oriented (Longitudinal-Transverse, [39]) specimens were used and test temperatures were chosen as -20 and -40 °C after preliminary tests for being close to both estimated T_0 and T_{28J} values. After charging the specimens were immersed in liquid nitrogen to await testing and were then moved to the alcohol bath that was cooled to the various test temperatures. The specimens were left in the alcohol bath for 30 minutes to warm up to the test temperatures and the temperature of each specimen was recorded before the tests. Fracture toughness tests were done in the alcohol bath, Fig. 4, and impact toughness tests in air. Thus, it was assumed that the H-charged specimens had exactly the same hydrogen levels as the small pieces used in the melt-extractions.

Fig. 4. Tested SENB specimen in an alcohol filled test rig on a tensile testing machine.

Fracture toughness tests and the determination of T_0 were performed according to the standard ASTM E1921 [12] with a constant displacement rate of 8.3E-3 mm/s using SENB specimens of a size 20 x 10 x 90 mm with an a/W ratio of 0.5 and a side-grooved 9 mm net thickness at the pre-fatigued crack front.

Charpy-V notch (CVN) impact testing was done according to the standard EN ISO 148-1 [40] using full-size 55 x 10 x 10 mm specimens, also at -60 °C and +20 °C using uncharged specimens, the latter to estimate the upper shelf toughness. Tanh-fitting introduced by Oldfield [41] was used to calculate the T_{28J} transition temperature values. For the curve fitting of the hydrogen charged CVN data the upper shelf toughness values of uncharged materials were used.

2.4. Microscopy

Microstructural characterization and measurements were carried out to study fractographic features and to assess the level of plastic deformation under predominantly brittle fracture fracture surfaces. A ZEISS Sigma field emission scanning electron microscope (FE-SEM) was used to study the fracture surfaces of SENB specimens. Cleavage fracture initiation sites were identified by following the river patterns on the fracture surfaces in regions narrowed down with the aid of a light optical stereo microscope. For selected specimens from the ATM material, the microstructure under these sites was revealed by preparing metallographic sections cut in the thickness direction and polished with the final polishing step done using a 0.04 μm diameter colloidal silica suspension. The microstructure and degree of deformation below the fracture surfaces right after the brittle fracture initiation sites were imaged using electron backscattered

diffraction (EBSD) measurements done with a 20 kV acceleration voltage and a 120 µm aperture with a 5000 x magnification and step size of 50 nm. An EDAX Hikari XP electron backscatter diffraction camera and accessory EDAX TSL OIM device were used for the measurements and analyses. A reference scan was also made in an unstressed area to determine the initial lattice distortion level. To clean up the data, points with a confidence index lower than 0.1 were excluded from the calculations, and grain confidence index standardization was used with a grain tolerance angle of 15° and a minimum grain size of 5 points. Kernel average misorientation analyses were then done to assess the level of plastic deformation using 5th nearest neighbours and a maximum misorientation of 3 degrees.

2.5. Modelling framework

The aforementioned three-step HE simulation was employed in this work. Briefly this procedure consists of:

(1) Elastic-plastic FE simulation. The specimen is loaded following the loading history in the experiment, yielding detailed information of the stress field.

(2) Stress-driven hydrogen diffusion analysis. The hydrogen profile is obtained by taking into account the hydrostatic stress gradient given in the first step.

(3) Elastic-plastic FE analysis with addition of user-defined cohesive elements inserted over the mid-section. The hydrogen concentration information obtained in the previous step is used to update the cohesive strength based on the HDL.

More specifically, the lattice hydrogen concentration is determined following a modified Fick's law [42], Eq. (3), where C_L is the lattice hydrogen concentration, D the diffusivity, V_H the partial molar volume of hydrogen in bcc ferrite, 2.1E-6 m^3/mol, R the gas constant, 8.314 J/mol, T_Z the absolute zero temperature and σ_h the local hydrostatic stress component. Initial hydrogen concentration C_I is assigned to every node in the model and the insulated boundary conditions are applied assuming that there is no significant hydrogen leak-out to the surrounding alcohol during the tests.

$$\frac{\partial C_L}{\partial t} = D\nabla^2 C_L + \frac{DV_H}{R(T-T_z)}\nabla C_L \nabla \sigma_h + \frac{DV_H}{R(T-T_z)}C_L \nabla^2 \sigma_h \tag{3}$$

The polynomial TSL originally proposed by Needleman [43], Eq. (4), is adopted in the CZM procedure. A convergence problem is frequently encountered in cohesive zone simulations [44]: at the point of instability, implicit FE computations are unable to converge to an equilibrium solution, which usually terminates the calculation and makes it impossible to follow the post-instability behaviour. In order to overcome this problem, the technique suggested by Gao and Bower [44] where a viscosity-like item is built into the constitutive behaviour of the cohesive elements, is applied, giving Eq. (5) for the viscosity regulated cohesive stress σ_v (Fig. 5.).

$$\sigma(\delta) = \begin{cases} \frac{27}{4}\sigma_c \frac{\delta}{\delta_c}\left(1-\frac{\delta}{\delta_c}\right)^2, \delta < \delta_c \\ 0, \delta > \delta_c \end{cases} \tag{4}$$

$$\sigma_v(\delta) = \sigma(\delta) + \zeta \frac{d}{dt}\left(\frac{\delta}{\delta_c}\right) \tag{5}$$
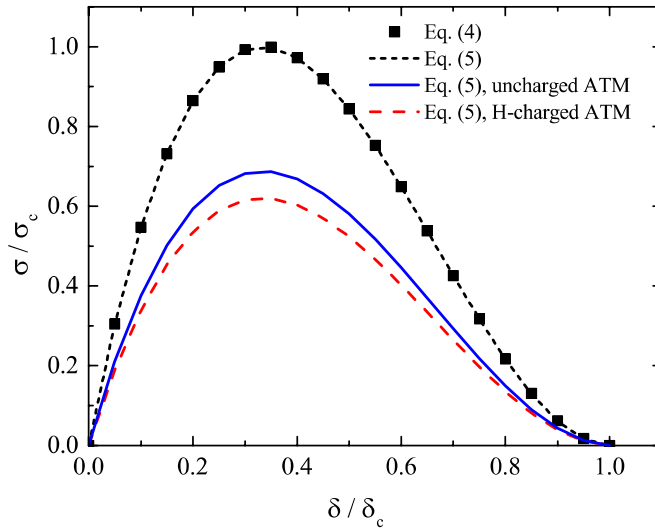
Fig. 5. Traction-separation law of Eq. (4) compared with the viscosity regulated cohesive stress of Eq. (5) using the measured hydrogen contents of the material ATM.

The CZM based hydrogen degradation law of Yu et al. [38] for martensitic AISI 4135 steel tempered at 360 °C, Eq. (2), is used here as being the closest representative of the materials in the current tests. The three-step simulation is realized in ABAQUS 6.14 with the cohesive process handled by a user element subroutine originally developed by Scheider [45]. Plane strain elements CPE4R are utilized in the mechanical analysis and mass diffusion elements DC2D4 in the hydrogen diffusion part. Only half of the specimen model is constructed due to symmetry. On the symmetry plane the symmetric opening of the cohesive elements is established by setting σ_c as half of the actual value and δ_c as the actual value [46,47]. Mesh refinement with a minimum element size of 10 μm is applied on the crack path to guarantee sufficient number of cohesive elements in the failure process zone as well as good resolution of the hydrogen profile.

2.6. Parameters for modelling

The material properties of ATM are used for the modelling due to its microstructural homogeneity. The stress – strain behaviour of the material at room temperature was taken as the average of that obtained using two tensile test specimens. For the elastic-plastic analyses, the stress – strain curve of the material at -20 °C was then obtained from the room temperature tensile test curve using Eq. (6) [11] assuming a power-law format. J2 flow theory with isotropic hardening is applied to describe the plastic flow. A power-law exponent of 0.1 is used to match the strength levels at the point of maximum load. Young's modulus is taken as 200 000 MPa and Poisson's ratio as 0.293.

$$\sigma_y(T) = \sigma_{ys} + \frac{5.56 \times 10^4\, MPaK}{T} - 189 MPa \qquad (6)$$

The initial hydrogen concentration assigned to each node is acquired from the melt-extraction results of both uncharged and hydrogen charged cases. The measured total hydrogen contents are considered in the calculations as readily diffusible lattice interstitial hydrogen and the influence of trapped hydrogen is excluded. This is justified with

the limited plasticity generated in high-strength steels before the failure, as done also in [48], and with a result that HE in the same tempered martensitic AISI 4135 can be described as a function of lattice hydrogen concentration and excluding the effects of trapped hydrogen [49]. Of course, neglecting plastic deformation and traps accumulated do not take into account the traps already existing in the microstructure rich in dislocations, carbides and variety of different types of grain boundaries. This is acknowledged and seen as a place for improvement in future studies.

Diffusion coefficients for low-carbon and medium-carbon as-quenched microstructures were collected from literature [18,50–54] to approximate the effective rate of diffusion of hydrogen for the materials used in this study: an average value of 2.3E-11 m^2/s at room temperature was obtained. To extrapolate this value to lower temperatures an Arrhenius type equation was fitted to the data for ferritic and martensitic steels reported in [55] giving Eq. (7) for as-quenched microstructures. This yields D_{eff} = 5.9E-12 m^2/s at -20 °C for the material ATM.

$$D_{eff} = 8 \times 10^{-8} exp \left(\frac{-20 \times 10^3}{RT} \right) m^2/s \tag{7}$$

Before the actual three-step procedure, a calibration of cohesive parameters against the average curve of the SENB tests at -20 °C had to be done on the model with cohesive elements but without hydrogen. The average CMOD and maximum load (F_{max}) values for the material ATM at -20 °C are used for the calibration to match the global behaviour by proper adjustment of the local behaviour of the cohesive elements. For the case of uncharged ATM containing 0.61 wppm hydrogen, parameters are δ_c = 0.014 mm and $\sigma_{c,H=0}$ = 2800 MPa, which is 2.5 times the calculated yield strength at -20 °C. A parameter study regarding the viscosity parameter ζ was done to keep its effect on both the local and global stress states at a negligible level while still enabling convergence. With $\zeta = 0$ simulations end in a convergence problem at the complete separation of the first cohesive element. The local shape of the force – CMOD curve during the separation of a cohesive element did not change when 1E-8 $\leqq \zeta \leqq$ 1E-3. A value of $\zeta = $ 1E-3 kept the calculation time at a reasonable level and that was therefore used in the third step analyses.

To broaden the applicability of the HE simulations, which in the experimental case have relatively fast constant rate displacement considering sufficient diffusion of hydrogen to further degrade the toughness properties, three different displacement rates were used to allow hydrogen more time to redistribute to the stressed areas: d = 8.3E-3 mm/s, equivalent to the experimental case, and reduced rates of 8.3E-6 mm/s and 8.3E-9 mm/s, corresponding roughly to test times of one minute, 17 hours and 694 days, respectively.

3. RESULTS

3.1. Toughness and fractography

The fracture toughness and impact toughness test results are summarized in Table 2 with their corresponding transition temperature values T_0 and T_{28J}. The data points and resultant analysis for T_0 are also shown in (Fig. 6). Fracture toughness results are presented as thickness corrected K_{Jc} equivalent to 1 inch thick specimens for the convenience of the reader and future comparability of the results.

Fracture toughness decreased 6 % on average in both materials due to hydrogen charging. Per case the change compared to the uncharged state were -4 % at -20 °C and -7 % at -40 °C for material ATM and -10 % at -20 °C and -2

% at -40 °C for material AB. Overall the material AB had on average 9 MPa√m or 9 % lower fracture toughness than the material ATM.

The total energy absorbed in impact toughness tests was 11 % lower on average with hydrogen charged specimens. While the absorbed energy dropped in other cases, AB had slightly higher value in the hydrogen charged state at -20 °C. The combined decrease in impact toughness due to charging was interestingly more pronounced at -40 °C with average decrease of 9 J/cm^2 compared to 0.5 J/cm^2 at -20 °C. Material ATM was clearly tougher than material AB with 21 J/cm^2 higher absorbed energy values.

Since toughness test results are well known to have significant scatter at the ductile-brittle transition temperature region and because tests were conducted at two different temperatures, transition temperature values are utilized to compare the results. In all of the cases both T_0 and T_{28J} values are elevated in hydrogen charged specimens. T_0 increases 8 °C for ATM and 6 °C for AB due to higher hydrogen content (Fig. 6). For both materials ATM and AB, the T_0 values between uncharged and hydrogen charged cases are statistically significantly different with respective p-values of 0.017 and 0.046 in two-tailed distributions using two-sample t-test assuming equal variances with the null hypothesis being that the means are equal. When impact toughness test data at -60 °C for the uncharged materials is included, T_{28J} increased with hydrogen charging by 17 °C for ATM and 10 °C for AB. However, when the data from -60 °C is left out and similar samples are compared, the T_{28J} decreases only 8 °C for ATM and 3 °C for AB (Table 2). These decreases in T_{28J} are statistically insignificant when tested the same way as above with corresponding p-values of 0.142 and 0.588 for materials ATM and AB, respectively. As regards the standard correlation between the T_0 and T_{28J}, estimates of T_0 for both ATM and AB are clearly off and extremely under-conservative.

Table 2. Average fracture toughness, average impact toughness, T_0 and T_{28J} values with their ± standard deviations and (numbers of parallels).

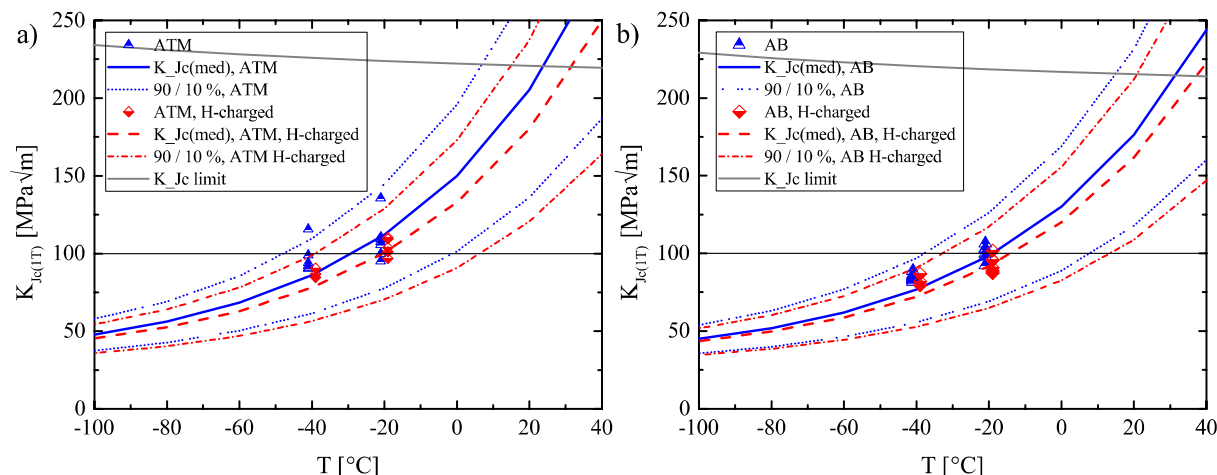|	$K_{Jc\ (1T)}$, -20°C [MPa√m]	$K_{Jc\ (1T)}$, -40°C [MPa√m]	T_0 [°C]	CVN total energy , -20°C [J/cm^2]	CVN total energy , -40 °C [J/cm^2]	T_{28J} [°C]
ATM, uncharged	109.1 ± 13.0 (7)	96.9 ± 9.7 (6)	-28 ± 6.4	64.3 ± 2.8 (3)	53.5 ± 1.5 (6)	-58 ± 10
ATM, H-charged	104.3 ± 5.6 (5)	87.3 ± 2.9 (3)	-20 ± 7.5	61.6 ± 1.5 (3)	44.9 ± 5.2 (3)	-50 ± 14
AB, uncharged	100.5 ± 4.9 (6)	84.7 ± 2.1 (8)	-19 ± 6.3	38.9 ± 5.5 (3)	35.1 ± 3.5 (6)	-40 ± 10
AB, H-charged	93.3 ± 5.4 (6)	82.7 ± 3.7 (3)	-13 ± 7.2	40.5 ± 0.1 (3)	25.6 ± 4.3 (3)	-37 ± 15

Fig. 6. Determination of fracture toughness reference temperature T_0 definition of uncharged and H-charged materials a) ATM and b) AB.

Fractography of the SENB specimens tested at -20 °C showed that the fracture surfaces of the ATM material were similar in both uncharged and hydrogen-charged conditions. Fracture morphology appears to be essentially brittle cleavage fracture separated by frequent bands of multi-void coalesced ductile fracture as seen in Fig. 7. In the uncharged specimens, where reliably identified, primary brittle fracture initiation sites are found to be located approximately 150 μm from the stretch zone, i.e. the part of the fracture surface that forms when the pre-fatigued crack initially starts to blunt under the applied load. Fracture surfaces of both conditions also show multiple secondary cracks, some small isolated intergranular surfaces and patches of "flat" fracture associated with hydrogen-related intergranular cracking, of which the latter two are more frequent in hydrogen charged specimens, Fig. 8. Fig. 7 b) shows brittle fracture initiated in a hydrogen charged specimen from an intergranularly cracked PAG and propagated in cleavage like manner. "Flat" features are present as shown in Fig. 8 a) and b). On a closer inspection, a lot of the H-charged cleavage surfaces have fine lath-like features that correspond to quasi-cleavage. With the aid of SEM-EDS analyses, in several cases TiN particles were identified in the immediate vicinity of the local brittle fracture initiation sites, Fig. 8 a).
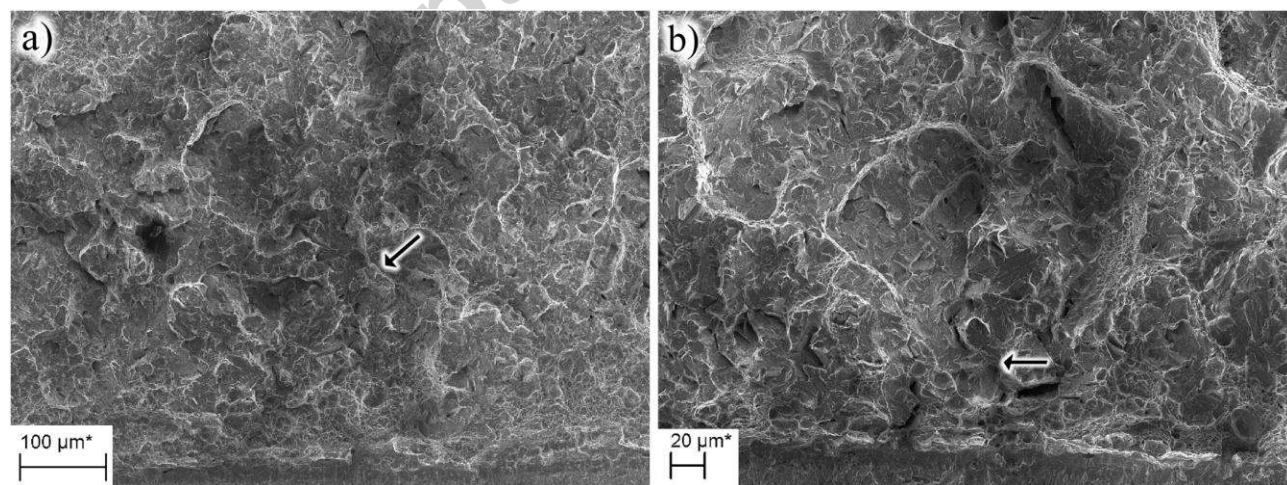

Fig. 7. Overview of the SENB fracture surfaces in a) uncharged ATM and b) hydrogen charged ATM. Black arrows show the possible brittle fracture initiation sites.
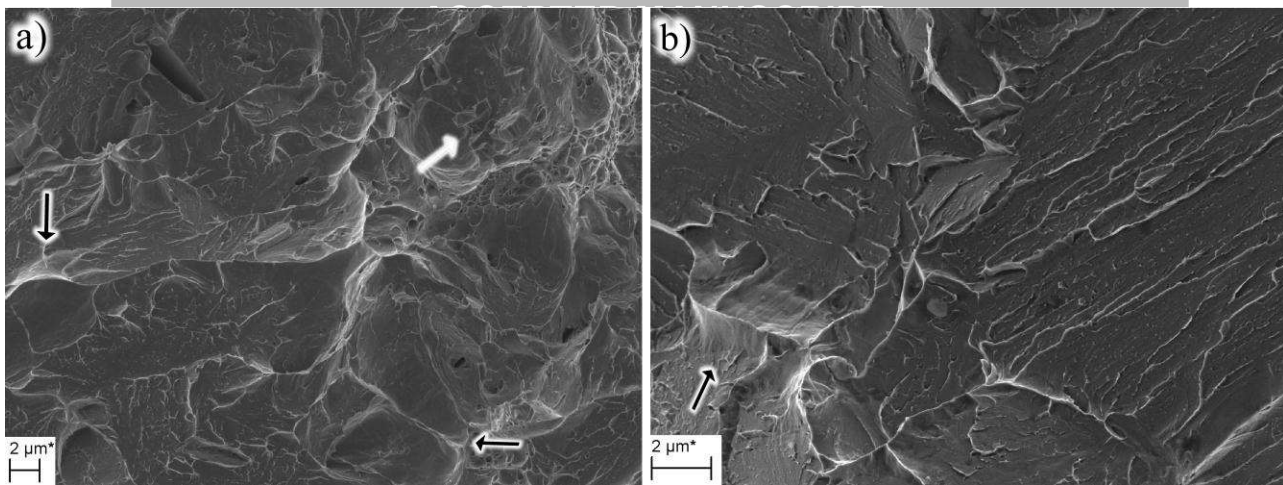
Fig. 8. Details of fracture surfaces of hydrogen charged ATM specimens a) local brittle fracture initiation site on a triple grain boundary at the centre of the picture, TiN inclusions (white arrow) and "flat" features, b) close-up of quasi-cleavage features. Black arrows point to flat features.

3.2. Kernel average misorientation measurements

Inverse pole figures and KAM maps are shown in Fig. 9 and the data of KAM maps of material ATM are plotted in Fig. 10 with average misorientation as a function of number fraction. Data accumulated from the region between the fracture surface and dashed lines shown in Fig. 9 are included in the calculations and number fraction is used to normalise the results. The lattice distortion or deformation is concentrated near the fracture surface and the area immediately below it, although colours corresponding to lattice distortion above zero are present throughout the measured area, Fig. 9 b) and d).

The KAM distributions for uncharged, hydrogen charged and a reference sample taken from an unstressed area are shown in Fig. 10. They show a distinctive peak at 1° that is characteristic of the given microstructure as a result of the contribution of lath boundaries [19]. This peak is the highest in the reference sample with the level of distortion being lower in other areas of the spectrum. The uncharged sample differs from the hydrogen-charged sample in that the level of distortion is clearly pronounced at levels under 0.5°, slightly bulging after 1.5° and the relative main peak is even lower. The overall difference is seen as higher lattice distortion in the uncharged sample and thus the hydrogen charged sample is considered to have experienced less plastic deformation in the region about 20 microns below the fracture surface.
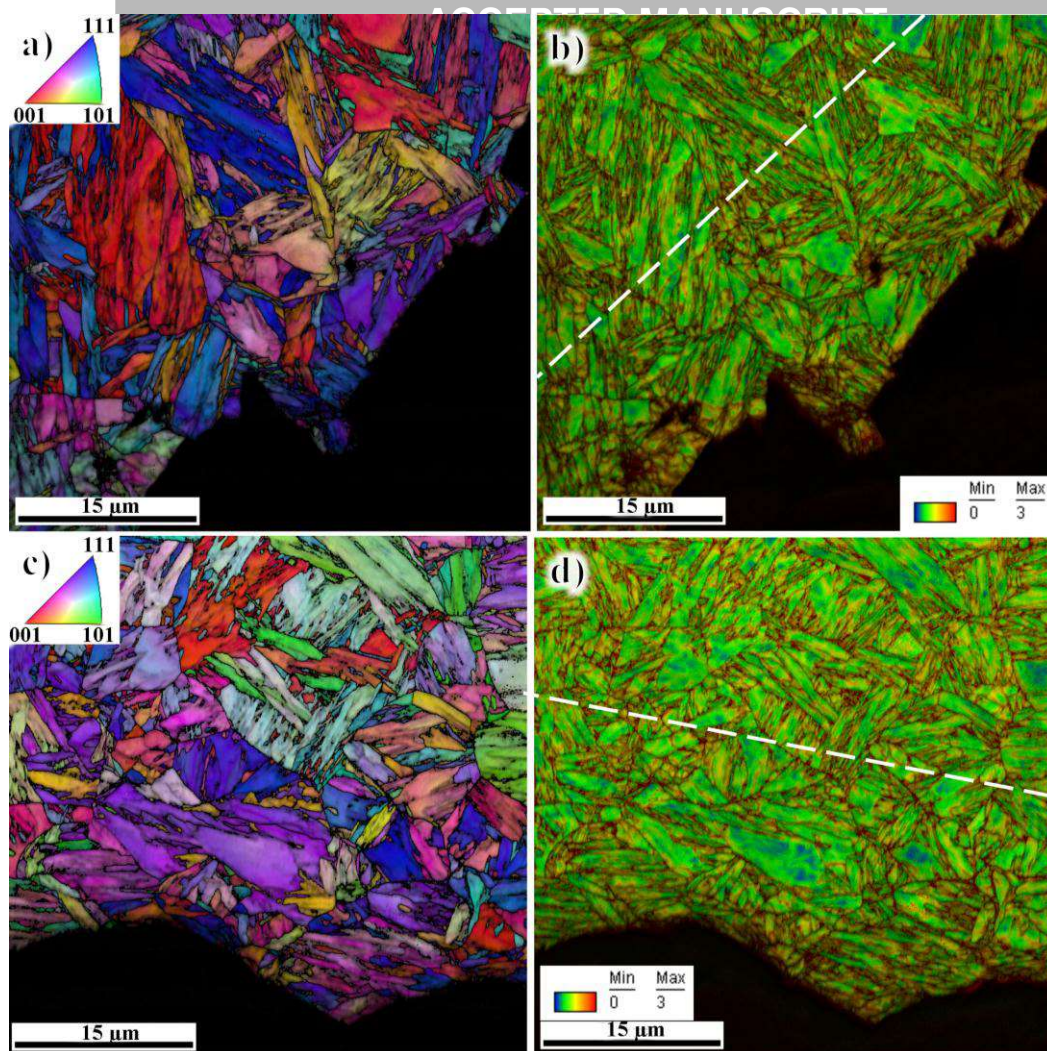
Fig. 9. a) inverse pole figure of ATM, b) KAM of ATM, c) inverse pole figure of ATM H-charged, d) KAM of ATM H-charged.
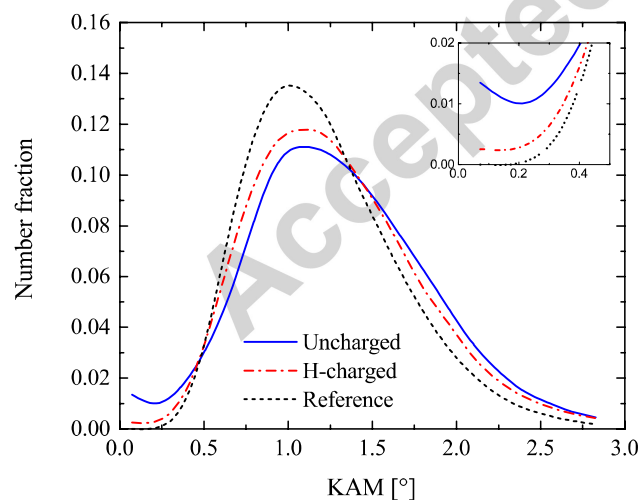

Fig. 10. Comparison of the KAM distributions for material ATM.

3.3. Cohesive zone modelling

Summaries of the modelling results are shown in Fig. 11 and Table 3. The point of failure in the model was based on the average distance of 150 μm of the brittle fracture initiation sites from the stretch zone in SENB specimens. In this way, failure is determined as the calculation step of complete separation of the tenth cohesive element, the point corresponding to crack growth of 100 μm. This point yields the maximum opening stress σ_{11} around the aforementioned average distance of the brittle fracture initiation sites. Experimental force – displacement behaviour is captured in a reasonable manner with the curves being at the average or the upper bound of the experiments.

For the uncharged case, satisfactory agreement is obtained between the model and experimental results with the predicted CMOD being 6 % lower, F_{max} 1 % higher and fracture toughness being 5 % lower than in the experiments. For the hydrogen charged case, the model predicts a more profound degradation of toughness, CMOD being -25 %, F_{max} -17 % and $K_{Jc(1t)}$ -20 % compared to the experimental results. According to the model, the fracture toughness decreases by 20 % at -20 °C with hydrogen charging. The same level of degradation is seen throughout the modelling results with the exception of maximum opening stress σ_{11}, which decreased just by 10 %.

When the simulated displacement rate is lowered from 8.3E-3 to 8.3E-6 mm/s, the predicted toughness properties decrease furher, on average 16 % in the uncharged case but just 8 % in the hydrogen-charged case. A much smaller effect is seen when the displacement rate is lowered to 8.3E-9 mm/s with the properties decreasing on average 4 % in the uncharged and less than 2 % in the hydrogen charged case. This implies that when the displacement rate is small enough, i.e. 8.3E-6 mm/s, hydrogen diffusion will be sufficient to allow the continuous achievement of the equilibrium concentration and therefore the deleterious effect of hydrogen saturates.
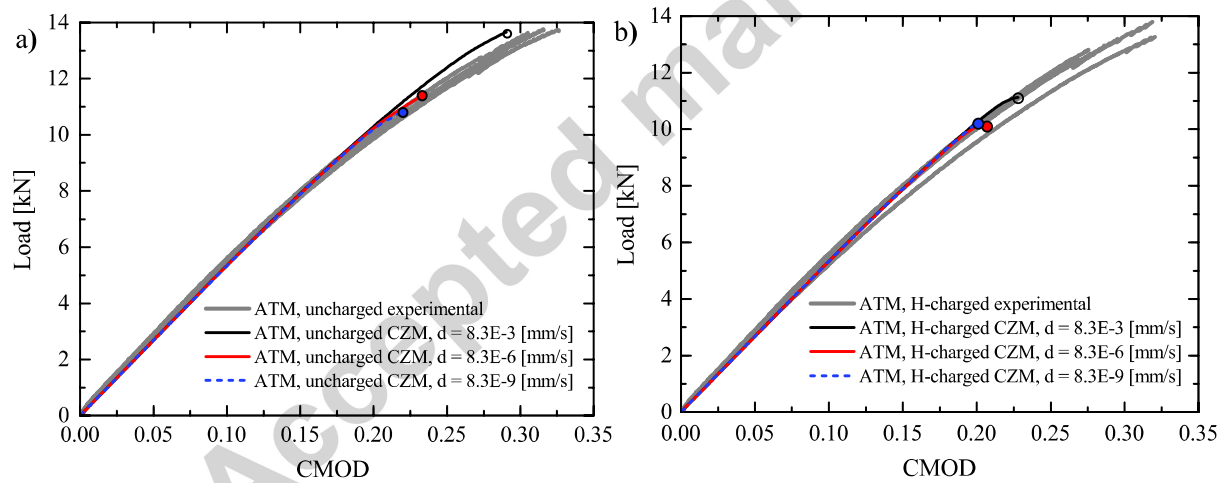

Fig. 11. CZM results with different diffusion rates of a) ATM, H = 0.61 ppm and b) H-charged ATM, H = 1.05 ppm.

Table 3. CZM results compared to experimental measurements at -20 °C (crack mouth opening displacement CMOD, maximum force at failure F_{max}, maximum opening stress σ_{11} and calculated fracture toughness $K_{Jc(1T)}$).

	CMOD [mm]	F_{max} [kN]	σ_{11} [MPa]	$K_{Jc(1T)}$ [MPa√m]
ATM, uncharged experimental average	0.309	13.5	-	109.1
ATM, H-charged experimental average	0.304	13.3	-	104.3
ATM, uncharged, d = 8.3E-3 mm/s	0.291	13.6	3 824	103.6
ATM, uncharged, d = 8.3E-6 mm/s	0.233	11.4	3 522	85.0

ATM, uncharged, d = 8.3E-9 mm/s	0.220	10.8	3 324	80.7
ATM, H-charged, d = 8.3E-3 mm/s	0.228	11.1	3 442	83.3
ATM, H-charged, d = 8.3E-6 mm/s	0.207	10.1	3 267	76.4
ATM, H-charged, d = 8.3E-9 mm/s	0.201	10.2	3 220	74.4

4. DISCUSSION

Combining toughness tests, microstructural characterization and hydrogen-informed finite element modelling, the findings lead to the outcome that higher hydrogen content is able to induce a reduction in toughness and deformation capabilities even in the quasi-static fracture toughness test at sub-zero temperatures. While there is no experimentally discernable effect of hydrogen charging on impact toughness at -20 or -40 °C, a significant elevation of the fracture toughness reference temperature T_0 is observed. This implies that hydrogen affects the $T_0 - T_{28J}$ correlation.

In the uncharged condition, material ATM contains a total of 0.6 ppm hydrogen, which actually corresponds to the value of $H_{c,D0.8}$ in Eq. (1) when the σ_{TS} of the ATM material (1354 MPa) is substituted in the equation. This means that 20 % of the ideal zero-hydrogen ductility is already lost with the material ATM the uncharged condition. Assuming that this loss in ductility translates into an equal loss in fracture toughness, for the material ATM, the hydrogen free $K_{Jc(1T)}$ would be 136 MPa√m at -20 °C and 130 MPa√m at -40 °C. Then the T_0 value for hydrogen free ATM would be -44 °C, 16 °C lower than with the uncharged hydrogen content of 0.6 wppm. If the HEDE is the main mechanism of degradation, as is assumed in the modelling, an assumption of a similar decrease in both fracture toughness and impact toughness is reasonable since the same scale of degradation of the cohesive energy is experienced in both cases with initial hydrogen contents in the beginning of the tests. Then the T_{28J} would be -63 °C, decreased by a mere 5 °C and 11 °C less than T_0. It is evident that a same decrease in toughness values in both tests causes a larger change in fracture toughness reference temperature T_0. This means that the shift in transition temperature values due to hydrogen could be a partial explanation to the $T_0 - T_{28J}$ correlation of low-carbon as-quenched martensitic steels, $T_0 = 0.8T_{28J} + 14$ °C, reported in Ref. [7] and considering the missing explanatory power of T_{28J}. In neither of these cases the estimates of standard correlation between the T_0 and T_{28J} changes but stays clearly unconservative. Both the correlation of Ref. [7] and the updated correlation of Wallin et al. [8] provide accurate estimates of T_0 in all four studied cases.

The measured smaller lattice distortion (KAM) in the hydrogen charged sample is in line with the overall decrease in fracture toughness. The distinctive peak in the KAM curves in Fig. 10 is most likely due to lath boundaries as shown by Morito et al [19] and in some unquantified part to martensitic transformation. As the result of deformation the peak shifts slightly towards higher misorientation angles while especially the lower tail raises and upper tail bulges out. Given the high number of data points per measurement, over 800 000 in each, the scatter is practically eliminated and small differences are captured with high confidence.
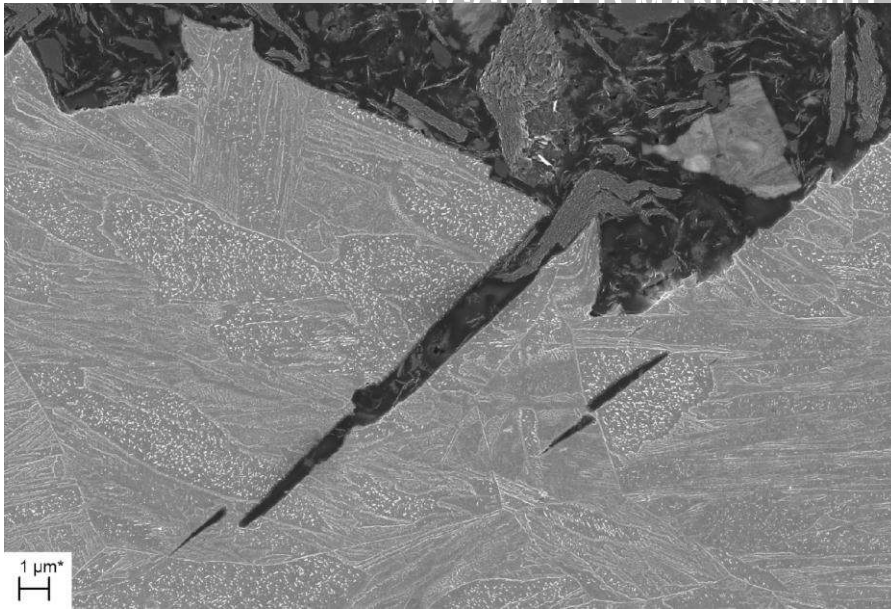
Fig. 12. Crack path and arrested secondary cracks in hydrogen charged ATM SENB specimen. Crack propagates from right to left.

An example of crack growth and secondary crack arrest in a hydrogen charged SENB sample is shown in Fig. 12, which is taken close to a brittle fracture initiation site. A difference is observed in the surface smoothness of the main and secondary cracks: the main crack surface contains many steps similar to what is seen in Fig. 8 b) and more pronounced where laths are almost parallel to the fracture surface, whereas the secondary cracks show completely flat surfaces. This constant small scale roughness could be quasi-cleavage as also shown in Refs. [22,28] while the secondary cracks are propagated in brittle cleavage manner with one coalesced neck in the largest one. Overall, the fracture surfaces are seen to consist of both brittle areas and ductile bands on their borders with the brittle areas showing features of cleavage fracture, quasi-cleavage and "flat" features. There is a higher incidence of hydrogen-related features with higher hydrogen content of the charged material ATM. Mixed fracture behaviour with subtle feature changes are seen to be caused by insufficient times for hydrogen to diffuse and "fully" embrittle the structure with the applied relatively fast displacement rates. Transgranular secondary cracks in Fig. 12 and other observed cases are arrested at the PAG boundary and high-angle sub-grain boundaries. Further study is needed to thoroughly investigate the fracture morphologies and mechanisms behind them, but this is outside the scope of this paper.

On the numerical aspect, satisfactory results are obtained with the three-step HE simulation procedure compared to the experimental data. Both the global and local failure behaviour are well captured in the uncharged experimental case, indicating that the hydrogen-informed cohesive zone technique is suited for modelling hydrogen embrittlement at low temperatures with proper adjustment of tensile properties and the effective diffusion coefficient. The model predicts a far greater decrease in toughness in the hydrogen-charged case than what is observed in the experiments. Regarding industrial applications, this conservative prediction could be regarded as beneficial. It should be re-emphasized that, in the hydrogen-assisted fracture model used here, hydrogen reduces the cohesive strength of user-defined elements on the predefined crack path with only the lattice hydrogen playing a role in diffusion, which can be considered reasonable since plasticity is negligible in high-strength steels at low temperatures [49]. This is also supported by the KAM observations discussed above. In this sense, the HDL of Yu et al. [38] is acceptable.

The reason for the conservative prediction observed in Fig. 11 b) might be caused by the omission, in the current model, of trapped hydrogen due to deformation and by the differing material characteristics used in the original calibration of the HDL. In any case, the effect of pre-existing filled traps has already been incorporated in the definition of effective hydrogen diffusion coefficient of trap-dense as-quenched microstructures acquired from the literature. What remains now unsolved are the amounts of trapped hydrogen. Determination of the diffusive hydrogen and further development of a hydrogen degradation law for as-quenched steels that can possibly tolerate higher hydrogen contents than quenched and tempered steels (Fig. 1) would be useful. Regarding the questions of local deformation characteristics and how much hydrogen is transported from the traps to the process zone, in-situ measurements [56,57] could provide additional information if the challenges associated with the very fine scale features of the martensitic microstructure can be overcome [57].

The displacement rate has an obvious effect on the failure initiation point and hydrogen concentration profile, as shown in Fig. 11. This can be rationalised by examining the hydrogen diffusion process as given in Fig. 13. The local hydrogen content is approximately two times higher with the original displacement rate at the given diffusion time, Fig. 13 b), thereby inducing more severe degradation on material strength. Further degradation is negligible since the level of degradation according to HDL saturates with ever increasing hydrogen content, as shown in Ref. [38]. Even with a relatively short time for hydrogen to diffuse to the stressed areas corresponding to the experimental case, Fig. 13 a), the difference in initial hydrogen contents is sufficient to decrease toughness properties. That is fully consistent with HEDE theory, modelling results, experiments and KAM measurements. However, it is worth keeping in mind that the same hydrogen contents would most likely be critical in highly stressed features at higher temperatures and real life service times as expected by the results shown in Fig. 1.
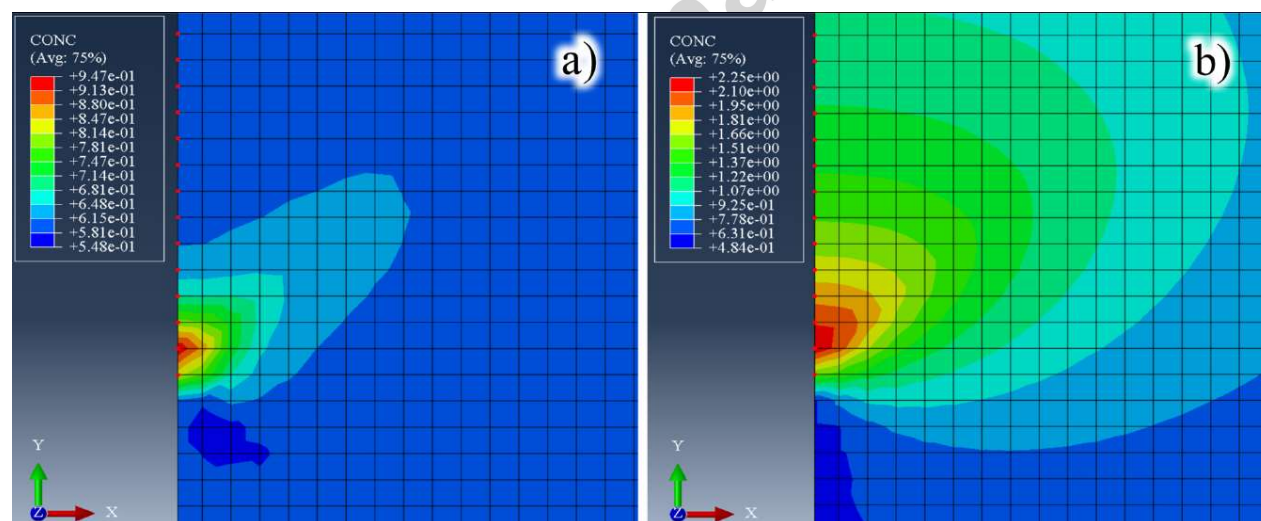

Fig. 13. Total hydrogen contents in mass diffusion analysis of uncharged ATM with effective diffusion coefficients corresponding to displacement rates of a) experimental 8.3E-3 mm/s, [0.548, 0.947] wppm and b) reduced 8.3E-6 mm/s, [0.48, 2.25] wppm.

5. CONCLUSIONS

The susceptibility of ultra-high-strength steel to hydrogen embrittlement has been studied in two as-quenched microstructures with standard fracture toughness and impact toughness tests in the transition temperature region at -

20 °C and -40 °C. Deformation under the fracture surfaces was measured and the experiments were modelled with hydrogen-informed cohesive zone modelling. In contrast to the general hypothesis that there would be no hydrogen-related problems at such low temperatures, it is shown that hydrogen embrittlement cannot be completely ignored under these circumstances. In the experiments fracture toughness decreased by 6 % in both materials and fracture toughness reference temperature T_0 showed a small but significant elevation of 8 °C and 6 °C in materials ATM and AB, respectively. The small decrease in fracture toughness is backed up by KAM measurements that show lower plastic deformation under the fracture surfaces with higher hydrogen content and by the three-step cohesive zone modelling that predicts an even higher decrease in toughness than what was observed experimentally. Absorbed energy in Charpy V impact testing was found to decrease with higher hydrogen content, but the observed changes were insignificant. The $T_0 - T_{28J}$ correlation changes slightly within the dataset, but stays unconservative in its conventional form. An effect of hydrogen on the transition temperature values is proposed where increasing hydrogen content separates the values further from each other. The results considering fracture toughness are consistent and it is concluded that hydrogen embrittlement is present and play a role, whether not dramatic, even at sub-zero temperatures in the studied cases.

References

[1]   M. Hemmilä, R. Liimatainen, T. Liimatainen, Hot-rolled Steel Strip and Method for Manufacturing the Same, EP1375694, 2004.

[2]   R. Hemmilä, M, Laitinen, T. Liimatainen, D. Porter, Mechanical and technological properties of ultra high strength Optim steels, in: Super High Strength Steels. Proceedings, 1st International Conference, Associazione Italiana di Metallurgia, Rome, Italy, 2005: p. 10.

[3]   A.J. Kaijalainen, P.P. Suikkanen, T.J. Limnell, L.P. Karjalainen, J.I. Kömi, D.A. Porter, Effect of austenite grain structure on the strength and toughness of direct-quenched martensite, Journal of Alloys and Compounds. 577 (2013) S642–S648. doi:10.1016/j.jallcom.2012.03.030.

[4]   Eurocode 3 - Design of steel structures Part 1-12, EN 1993-1-12, Additional rules for the extension of EN 1993 up to steel grades S 700, 2007.

[5]   K. Wallin, A Simple Theoretical Charpy V - KIC Correlation for Irradiation Embrittlement. Innovative Approaches to Irradiation Damage and Fracture Analysis, in: PVP 170, ASME, 1989: pp. 93–100.

[6]   P. Nevasmaa, P. Karjalainen-Roikonen, A. Laukkanen, T. Nykänen, A. Ameri, T. Björk, et al., Fracture characteristics of new ultra- high-strength steel with yield strengths 900 - 960 MPa, in: 2nd Int. Conference on Super-High Strength Steels, Associazione Italiana di Metallurgia, Verona, Italy, 2010.

[7]   S. Pallaspuro, T. Limnell, P. Suikkanen, D. Porter, T0 − T28J Correlation of Low-carbon Ultra-high-strength Quenched Steels, Procedia Materials Science. 3 (2014) 1032–1037. http://www.sciencedirect.com/science/article/pii/S2211812814001692.

[8]   K. Wallin, S. Pallaspuro, I. Valkonen, P. Karjalainen-Roikonen, P. Suikkanen, Fracture properties of high performance steels and their welds, Engineering Fracture Mechanics. 135 (2015) 219–231. doi:10.1016/j.engfracmech.2015.01.007.

[9]   EN 1993-1-10, Eurocode 3: Design of steel structures - Part 1-10: Material toughness and through-thickness properties, 2005.

[10]   SINTAP, Structural Integrity Assessment Procedures for European Industry - Final Procedure, Report No. BE95-1426/FR/7, 1999.

[11]   FITNET, FITNET Fitness-for-Service (FFS) − Procedure (Volume I), Revision M, European Thematic Network FITNET, Geesthacht, 2008. http://www.eurofitnet.org/Section0-Intro.pdf.

[12]   ASTM, ASTM E1921-14a Standard Test Method for Determination of Reference Temperature, T0, for ferritic Steels in the Transition Range, 2015. doi:10.1520/E1921-05.

[13]   M. Tvrdy, V. Suchanek, L. Hyspecka, K. Mazanek, Effect of metallurgy on stress corrosion cracking and hydrogen embrittlement of ultrahigh strength steels, in: D. Taplin (Ed.), Advanced Research on the Strength and Fracture of Materials, 4th International Conference on Fracture, University of Waterloo Press, Waterloo, 1977: pp. 255–59. https://books.google.no/books?id=_DgvBQAAQBAJ&pg=PA255&lpg=PA255&dq=Effect+of+metallurgy+on+stress+corr osion+cracking+and+hydrogen+embrittlement+of+ultrahigh+strength+steels&source=bl&ots=ijIyhY-IYt&sig=KN6p2WGcZcSuNGmxQ7lGI9Ztq-4&hl=fi&sa=X&ved=0ahUKEwjO.

[14]   S. Matsuoka, STX-21 Project, 2002. www. nims.go.ip.

[15]   O. Wang, S. Adolfsson, T. Siwecki, Critical Hydrogen Level for Mechanical Property Degradation of High Strength Steels, Swedish Institute for Metals Research. Report No: (2004).

[16]   Wang X.T., T. Siwecki, Study on Susceptibility of Hydrogen Embrittlement in a Tool Steel, Materials Science Forum.

(2007) 103–106. http://zh.scientific.net/MSF.561-565.103.pdf (accessed May 30, 2016).

[17]   M. Wang, E. Akiyama, K. Tsuzaki, Hydrogen degradation of a boron-bearing steel with 1050 and 1300MPa strength levels, Scripta Materialia. 52 (2005) 403–408. doi:10.1016/j.scriptamat.2004.10.023.

[18]   V. Olden, A. Alvaro, O.M. Akselsen, Hydrogen diffusion and hydrogen influenced critical stress intensity in an API X70 pipeline steel welded joint – Experiments and FE simulations, International Journal of Hydrogen Energy. 37 (2012) 11474–11486. doi:10.1016/j.ijhydene.2012.05.005.

[19]   S. Morito, X. Huang, T. Furuhara, T. Maki, N. Hansen, The morphology and crystallography of lath martensite in alloy steels, Acta Materialia. 54 (2006) 5323–5331. doi:10.1016/j.actamat.2006.07.009.

[20]   R.A. Oriani, A mechanistic theory of hydrogen embrittlement of steels, Berichte Der Bunsengesellschaft Für Physikalische Chemie. 76 (1972) 848–857. doi:10.1002/bbpc.19720760864.

[21]   H.K. Birnbaum, P. Sofronis, Hydrogen-enhanced localized plasticity—a mechanism for hydrogen-related fracture, Materials Science and Engineering: A. 176 (1994) 191–202. doi:10.1016/0921-5093(94)90975-X.

[22]   A. Nagao, C.D. Smith, M. Dadfarnia, P. Sofronis, I.M. Robertson, The role of hydrogen in hydrogen embrittlement fracture of lath martensitic steel, Acta Materialia. 60 (2012) 5182–5189. doi:10.1016/j.actamat.2012.06.040.

[23]   A. Nagao, C.D. Smith, M. Dadfarnia, P. Sofronis, I.M. Robertson, Interpretation of Hydrogen-induced Fracture Surface Morphologies for Lath Martensitic Steel, Procedia Materials Science. 3 (2014) 1700–1705. doi:10.1016/j.mspro.2014.06.274.

[24]   A. Shibata, H. Takahashi, N. Tsuji, Microstructural and Crystallographic Features of Hydrogen-related Crack Propagation in Low Carbon Martensitic Steel, ISIJ International. 52 (2012) 208–212. doi:10.2355/isijinternational.52.208.

[25]   Y.-H. Kim, H.J. Kim, J.W. Morris, The influence of precipitated austenite on hydrogen embrittlement in 5.5Ni steel, Metallurgical Transactions A. 17 (1986) 1157–1164. doi:10.1007/BF02665314.

[26]   A. Shibata, T. Murata, H. Takahashi, T. Matsuoka, N. Tsuji, Characterization of Hydrogen-Related Fracture Behavior in As-Quenched Low-Carbon Martensitic Steel and Tempered Medium-Carbon Martensitic Steel, Metallurgical and Materials Transactions A: Physical Metallurgy and Materials Science. 46 (2015) 5685–5696. doi:10.1007/s11661-015-3176-x.

[27]   C.J. McMahon, Hydrogen-induced intergranular fracture of steels, Engineering Fracture Mechanics. 68 (2001) 773–788. doi:10.1016/S0013-7944(00)00124-7.

[28]   M.L. Martin, J.A. Fenske, G.S. Liu, P. Sofronis, I.M. Robertson, On the formation and nature of quasi-cleavage fracture surfaces in hydrogen embrittled steels, Acta Materialia. 59 (2011) 1601–1606. doi:10.1016/j.actamat.2010.11.024.

[29]   M.L. Martin, I.M. Robertson, P. Sofronis, Interpreting hydrogen-induced fracture surfaces in terms of deformation processes: A new approach, Acta Materialia. 59 (2011) 3680–3687. doi:10.1016/j.actamat.2011.03.002.

[30]   S.I. Wright, M.M. Nowell, D.P. Field, A Review of Strain Analysis Using Electron Backscatter Diffraction, Microscopy and Microanalysis. 17 (2011) 316–329. doi:10.1017/S1431927611000055.

[31]   W.S. Li, H.Y. Gao, H. Nakashima, S. Hata, W.H. Tian, In-situ study of the deformation-induced rotation and transformation of retained austenite in a low-carbon steel treated by the quenching and partitioning process, Materials Science and Engineering: A. 649 (2016) 417–425. doi:10.1016/j.msea.2015.09.076.

[32]   M.A. Mohtadi-Bonab, M. Eskandari, J.A. Szpunar, Texture, local misorientation, grain boundary and recrystallization fraction in pipeline steels related to hydrogen induced cracking, Materials Science and Engineering: A. 620 (2015) 97–106. doi:10.1016/j.msea.2014.10.009.

[33]   Z. Lu, T. Shoji, F. Meng, H. Xue, Y. Qiu, Y. Takeda, et al., Characterization of microstructure and local deformation in

316NG weld heat-affected zone and stress corrosion cracking in high temperature water, Corrosion Science. 53 (2011) 1916–1932. doi:10.1016/j.corsci.2011.02.009.

[34]   V. Olden, C. Thaulow, R. Johnsen, E. Østby, Cohesive zone modeling of hydrogen-induced stress cracking in 25% Cr duplex stainless steel, Scripta Materialia. 57 (2007) 615–618. doi:10.1016/j.scriptamat.2007.06.006.

[35]   V. Olden, C. Thaulow, R. Johnsen, E. Østby, T. Berstad, Application of hydrogen influenced cohesive laws in the prediction of hydrogen induced stress cracking in 25%Cr duplex stainless steel, Engineering Fracture Mechanics. 75 (2008) 2333–2351. doi:10.1016/j.engfracmech.2007.09.003.

[36]   A. Needleman, Some Issues in Cohesive Surface Modeling, Procedia IUTAM. 10 (2014) 221–246. doi:10.1016/j.piutam.2014.01.020.

[37]   S. Serebrinsky, E. Carter, M. Ortiz, A quantum-mechanically informed continuum model of hydrogen embrittlement, Journal of the Mechanics and Physics of Solids. 52 (2004) 2403–2430. doi:10.1016/j.jmps.2004.02.010.

[38]   H. Yu, J.S. Olsen, A. Alvaro, V. Olden, J. He, Z. Zhang, A uniform hydrogen degradation law for high strength steels, Engineering Fracture Mechanics. 157 (2016) 56–71. doi:10.1016/j.engfracmech.2016.02.001.

[39]   ASTM, ASTM E1823-13, Standard Terminology Relating to Fatigue and Fracture Testing, 1998. doi:10.1520/E1823-13.2.

[40]   EN ISO 148-1, Metallic Materials, Charpy pendulum impact test, Part 1: Test method, 2010.

[41]   W. Oldfield, Curve fitting impact test data: a statistical procedure, ASTM Standardization News. 3 (1975) 24–29.

[42]   ABAQUS User Manual, Version 6.14-1, Dassault Systemes Simulia Corp., Providence, RI; 2014, (n.d.).

[43]   A. Needleman, A Continuum Model for Void Nucleation by Inclusion Debonding, Journal of Applied Mechanics. 54 (1987) 525. doi:10.1115/1.3173064.

[44]   Y.F. Gao, A.F. Bower, A simple technique for avoiding convergence problems in finite element simulations of crack nucleation and growth on cohesive interfaces, Modelling and Simulation in Materials Science and Engineering. 12 (2004) 453–463. doi:10.1088/0965-0393/12/3/007.

[45]   I. Scheider, Cohesive model for crack propagation analyses of structures with elastic − plastic material behavior - Foundations and implementation, Geesthacht, 2001.

[46]   W. Brocks, D. Arafad, M. M, Exploiting symmetries of fe models and application to cohesive elements, Milano / Kiel, 2013.

[47]   H. Yu, J.S. Olsen, V. Olden, A. Alvaro, J. He, Z. Zhang, Viscous regularization for cohesive zone modeling under constant displacement: An application to hydrogen embrittlement simulation, Engineering Fracture Mechanics. 166 (2016) 23–42. doi:10.1016/j.engfracmech.2016.08.019.

[48]   M. Wang, E. Akiyama, K. Tsuzaki, Effect of hydrogen and stress concentration on the notch tensile strength of AISI 4135 steel, Materials Science and Engineering: A. 398 (2005) 37–46. doi:10.1016/j.msea.2005.03.008.

[49]   C. Ayas, V.S. Deshpande, N.A. Fleck, A fracture criterion for the notch strength of high strength steels in the presence of hydrogen, Journal of the Mechanics and Physics of Solids. 63 (2014) 80–93. doi:10.1016/j.jmps.2013.10.002.

[50]   B. Hutchinson, A. Bengtson, Hydrogen in Steels – a Literature Study, Swedish Institute for Metals Research. Report No: (2002).

[51]   S.L.I. Chan, Hydrogen trapping ability of steels with different microstructures, Journal of the Chinese Institute of Engineers. 22 (1999) 43–53. doi:10.1080/02533839.1999.9670440.

[52]   W.C. Luu, J.K. Wu, The influence of microstructure on hydrogen transport in carbon steels, Corrosion Science. 38 (1996) 239–245. doi:10.1016/0010-938X(96)00109-6.

[53]   E. Hörnlund, J.K.T. Fossen, S. Hauger, C. Haugen, T. Havn, T. Hemmingsen, et al., Hydrogen Diffusivities and Concentrations in 520M Carbon Steel under Cathodic Protection in 0.5M NaCl and the Effect of Added Sulphite, Dithionite, Thiosulphate, and Sulphide, International Journal of Electrochemical Science. 2 (2007) 82–92. http://pdf.easechem.com/pdf/07/2010082.pdf (accessed March 5, 2015).

[54]   N. Parvathavarthini, S. Saroja, R.K. Dayal, Influence of microstructure on the hydrogen permeability of 9%Cr–1%Mo ferritic steel, Journal of Nuclear Materials. 264 (1999) 35–47. doi:10.1016/S0022-3115(98)00486-3.

[55]   T. Böllinghaus, H. Hoffmeister, C. Middel, Scatterbands for hydrogen diffusion coefficients in steels having a ferritic or martensitic microstructure and steels having an austenitic microstructure at room temperature, Welding in the World. 1 (1996) 16–23.

[56]   I.M. Robertson, The effect of hydrogen on dislocation dynamics, Engineering Fracture Mechanics. 68 (2001) 671–692. doi:10.1016/S0013-7944(01)00011-X.

[57]   A. Barnoush, H. Vehoff, Recent developments in the study of hydrogen embrittlement: Hydrogen effect on dislocation nucleation, Acta Materialia. 58 (2010) 5274–5285. doi:10.1016/j.actamat.2010.05.057.